



Fibre Orientation Modelling Applied to Contracting Flows Related to Papermaking

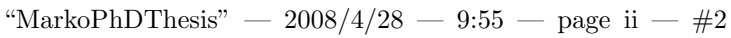
by

Marko Hyensjö

May 2008
Doctoral Thesis from
Royal Institute of Technology
Department of Mechanics
SE-100 44 Stockholm, Sweden









Akademisk avhandling som med tillstånd av Kungliga Tekniska Högskolan i Stockholm framlägges till offentlig granskning för avläggande av teknologie doktorsexamen torsdagen den 5:e juni 2008 kl 10.00 i sal L1, Kungliga Tekniska Högskolan, Drottning Kristinas väg 30, Stockholm.

©Marko Hyensjö 2008

Tryck: Universitetsservice US AB, Stockholm 2008









Fibre Orientation Modelling Applied to Contracting Flows Related to Papermaking

Marko Hyensjö 2008

Department of Mechanics, Royal Institute of Technology SE-100 44 Stockholm, Sweden.

Abstract

The main goal of this work was to develop numerical models for studying the behaviour of fibres in an accelerated flow. This is of special interest for e.g. papermaking. The early stage of the paper manufacturing process determines most of the final properties of a paper sheet. The complexity of studying the flow of fibre suspensions both experimentally and numerically emphasises a need for new ideas and developments.

By means of solving the evolution of a convective-dispersion equation, *i.e.* the Fokker-Planck equation, a fully 3D approach with respect to the position and the two fibre angles, polar and azimuthal angles, following a streamline is presented. As an input to the fibre orientation model the turbulent flow field is solved by Computational Fluid Dynamics (CFD) with second-order closure in the turbulence model. In this work two new hypotheses have been presented for the variation of the non-dimensional rotational diffusivity with non-dimensional fibre length, L_f/η , and the Reynolds number based on the Taylor micro-scale of the turbulence, Re_{λ} . Parameters for the two new hypotheses and earlier models are determined with the aim of achieving a general relation and a value of the rotational dispersion coefficient of stiff fibres in an anisotropic turbulent fluid flow. Earlier modelling work has been focused on solving the planar approach, *i.e.* assuming all fibres to be in one plane. This planar approach is discussed and compared with the fully 3D approach and its validity is evaluated.

The optimization of parameters for the different hypotheses correlated on a central streamline, showed a good agreement with an independent experimental result in the undisturbed region. Moreover, it is particularly interesting that the boundary layer region and the wake region are predicted fairly well and the phenomena are well described, which has not been the case earlier. It seems that the new hypothesis based on the variation of the non-dimensional fibre length, L_f/η gives the best correlation in these shear-layer regions. Furthermore it was established that the planar approach fails to predict shear layers, i.e. the boundary layer and the wake regions. As emphasized in the theory section, the planar formulation is strictly valid only if all fibres are oriented in one plane, which is not the case in the shear layers. In the undisturbed region, the 3D and the planar approaches, agree in their results. This leads to the conclusion that both approaches are suitable when shear layers are not studied.

Descriptors: Fokker-Planck, fibre orientation, shear flow, fibre suspension, planar contraction, headbox, turbulent flow, anisotropy







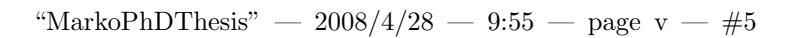
 "Marko Ph
D
Thesis" — 2008/4/28 — 9:55 — page iv — #4



iv













The Height of Curiosity:

Mother - "Don't ask so many questions, child. Curiosity killed the cat." Willie - "What did the cat want to know, Mom?"

The Portsmouth Daily Times, March 1915







 "Marko Ph
D
Thesis" — 2008/4/28 — 9:55 — page vi
 — #6



vi









Preface

This thesis deals with numerical modelling of the early stage of the paper-making process, called the forming section. This is basically the stage where a continuous web of interlocked fibres is formed, after removing the "loose" water between the fibres and fibre agglomerates. The principle behaviour, *i.e.* orientation, of fibres suspended in water and accelerated towards the papermachine speed is targeted in this study. This research work was conducted within a framework of a industrial PhD work between Metso Paper Karlstad AB and Royal Institute of Technology (KTH) in Stockholm.

The thesis is divided into an introduction to papermaking in general and in particular the forming section. Then follows a summary of the theory, methods, results and conclusion covered in the five appended scientific papers.

Karlstad, May 2008 Marko Hyensjö

Appended papers:

- Paper 1. Hyensjö, M., Dahlkild, A., Krochak, P., Olson, J. and Hämäläinen, J., 2007, Modelling the Effect of Shear Flow on Fibre Orientation Anisotropy in a Planar Contraction. Nordic Pulp and Paper Research Journal, 22(3):376-382.
- Paper 2. Hyensjö, M. and Dahlkild, A., 2008, Study of the Rotational Diffusivity Coefficient of Fibres in Planar Contracting Flows with Varying Turbulence Levels. International Journal of Multiphase Flow, article in press, available online at www.sciencedirect.com, doi:10.1016/j.ijmultiphaseflow.2008.02.005.
- **Paper 3.** Hyensjö, M., Dahlkild, A. and Wikström, T., Evolution of the Rotational Diffusivity Coefficient of Fibres along the Centreline of Turbulent Planar Contracting Flows. To be submitted
- **Paper 4.** Hyensjö, M., Dahlkild, A. and Wikström, T., Modeling the Fibre Anisotropy Profile in Shear Layers Leaving a Planar Contraction. To be submitted
- **Paper 5.** Hyensjö, M., Dahlkild, A. and Wikström, T., Comparison between Planar and Fully 3D Approaches for the Evolution of Fibre Orientation in the Shear Layers of Planar Contractions. To be submitted









viii PREFACE

Division of work between authors

Paper 1: Numerical algorithms and implementation were developed by Marko Hyensjö(MH) assisted by Paul Krochak (PK). The ideas behind the paper are contributions from all the authors. MH prepared the manuscript and with comments and discussion with Anders Dahlkild (AD) and the other authors.

Paper 2: Modelling and implementation were carried out by MH under the guidance of AD. The ideas behind the paper are contribution from both authors. The manuscript was prepared by MH with support from, discussion with and the guidance of AD.

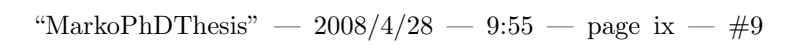
Paper 3: Modelling and implementation were carried out by MH under the guidance of AD and Tomas Wikström (TW). The ideas behind the paper are contribution from all the authors. MH prepared the manuscript with comments from and discussion with the other authors.

Paper 4: Modelling and implementation were carried out by MH under the guidance of AD and TW. The ideas behind the paper are contribution from all the authors. MH prepared the manuscript with comments from and discussion with the other authors.

Paper 5: Modelling and implementation were carried out by MH under the guidance of AD and TW. The ideas behind the paper are contribution from all the authors. MH prepared the manuscript with comments from and discussion with the other authors.











Contents

Prefac	ee	vii
Chapt	er 1. Introduction	1
1.1.	Introduction to Papermaking	1
1.2.	Scope of Thesis	3
1.3.	Outline of Thesis	3
Chapt	er 2. Theory	5
2.1.	Fluid Mechanics	5
2.2.	Fibre Suspensions	7
2.3.	Full 3D Formulation of the Fibre Orientation Model	9
2.4.	Planar Formulation of the Fibre Orientation Model	10
2.5.	Rotational Dispersion Coefficient	11
Chapt	er 3. Purpose and Methods	16
3.1.	Paper 1	16
3.2.	Paper 2	17
3.3.	Paper 3	18
3.4.	Paper 4 and Paper 5	18
\mathbf{Chapt}	er 4. Results	21
Chapt	er 5. Concluding Remarks	30
Ackno	wledgements	32
Bibliography		







 "Marko Ph
D
Thesis" — 2008/4/28 — 9:55 — page x — #10



x CONTENTS









CHAPTER 1

Introduction

The purpose of this introduction is to give an overview of the work covered in this thesis. Furthermore the aim is to guide the reader to put this work into its context in the research area of papermaking. This highly multidisciplinary research field covers *e.g.* paper mechanics, fluid mechanics, physics, chemical engineering, chemistry and automation. The many disciplines are highly dependent on each other, which increases the complexity. Therefore attempts are made to isolate the basic physics of some particular phenomena that separately are critically dependent on only a smaller number of parameters. This knowledge is then used to interpret the final paper properties.

1.1. Introduction to Papermaking

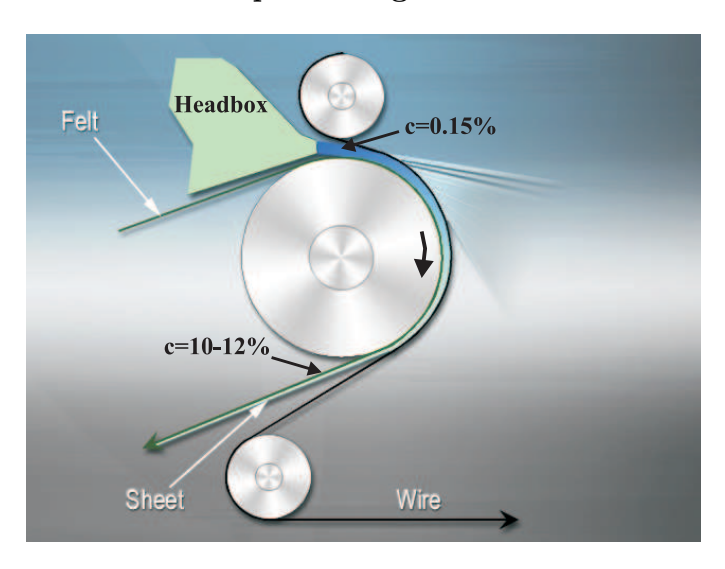


FIGURE 1.1. Principle of twin wire former for Tissue paper grades: Headbox with conventional Crescent former.

The process of papermaking converts a suspension consisting of cellulose fibres and water into a continuous dry paper web or sheet. A typical dry paper sheet consists of cellulose fibres, fines, chemicals and some fillers such as clay. The process of producing such a sheet at a high production level at minimum











2 1. INTRODUCTION

cost, with high demands on quality with respect to strength or dimensional stability, is an obvious challenge. Also today the energy perspective is evident and sets new horizons for the art of papermaking. This naturally drives the technology development and new insights are needed. Additional and deeper knowledge of the physics involved in the process is essential, which in turn also can lead to new process solutions. One of the key components of a paper machine is the forming section, figure 1.1. Here the fibre suspension, e.g. fibres, chemicals, fillers etc., undergoes the process from being relative fluid to relative solid as water between fibres and agglomerates of fibres, are removed in a somewhat controlled manner. Thus in figure 1.1 the concentration by weight, c, goes from 0.15% to 10-12% in the dewatering zone removing about 95% of the water. It results in a sufficiently interlaced strong fibre mat or sheet that holds together, where the fibres are interlocked, as it continues in the process. Pressing and drying follow, with the main purpose of removing the remaining water inside the hollow fibres and in the fibre walls. Since cellulose fibre is an organic material and its properties are highly dependent on water content, the control of the process as the paper web dries is important, which in turn also effects the final paper properties. The first part of the forming section, called



FIGURE 1.2. View of a Tissue headbox for a twin wire former.

the headbox, ensures an even distribution of the fibre suspension for widths up to over 10m, with a jet thickness of about 10mm leaving this headbox. The concentration, c, of the fibre suspension in the headbox varies, depending









1.3. OUTLINE OF THESIS

3

on the paper grade, between 0.15% to 1 % by weight. Note that the volume concentration can be up to twice the mass concentration depending on the fibre coarseness and the degree of swelling. In detail the headbox consists of two major parts, first a bundle of tubes with step expansions, referred to as the turbulence generator, and second a contraction, which accelerates the fibre suspension to jet velocities up to 35 m/s, cf. figure 1.2. The flow distributer connected just before the headbox ensures an even pressure distribution across the machine width, thus giving a constant flow rate. The distributer is not shown in figure 1.2. The quality of the paper, e.g. the strength, is largely dependent on the early process steps. The contraction section increases the degree of orientation of the fibres and agglomerates of fibres, giving anisotropic strength properties to the paper, e.g. Nordström & Norman (1994). The formation, i.e. small-scale basis weight variation, is dependent on the state of fibre suspension in this forming section. To ensure a good formation the fibres must be evenly dispersed in the suspension. The paper strength properties in the machine direction and cross-machine direction as well as in the thickness direction are important for runnability and dimensional stability of the paper sheet in copying and printing machines. The strength properties are determined by chemicals, fibre type and preparation, but also largely by anisotropy of fibre orientation distribution, e.q. Leppänen et al. (2005). Many of the final paper properties are based upon the state of the fibre suspension in the early stage of the process, e.g. Norman & Söderberg (2001).

1.2. Scope of Thesis

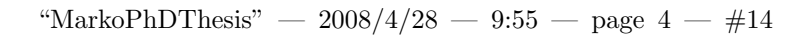
There are many aspects of the physics in the forming section that have not yet been explained and new challenges are revealed as we proceed towards higher machine speeds. Theoretical as well as experimental studies of fibre suspensions are very complex. This drives both numerical and experimental research hand in hand to reveal the further details of the problem. This study emphasises the need of knowledge in the area of the headbox and particularly the planar contraction section. This modelling work is focused on how accelerated flow, wall boundaries, wakes and turbulence level influence fibre orientation. The results provides a better basis for the design of paper machine equipment or guiding instructions for paper producers. The main target was to develop a numerical model that accounts for turbulence and shear flow, i.e. boundary layer or wake, on fibre orientation for a typical headbox contraction geometry. In particular, model parameters of the rotational diffusivity are determined by comparison to available experimental data. The work also points out the importance of choice of a proper modelling strategy depending on where the analysis is made in the planar contraction.

1.3. Outline of Thesis

The first part of the thesis consists of a summary of the papers covered and the second part consists of the appended papers. The main part of this work











is covered in the five appended papers. In paper 1 the planar approach to the fibre orientation distribution function is studied. In paper 2 a 3D fibre orientation model, together with two new hypotheses for the rotational diffusivity coefficient, is presented. Further, coefficients for the hypotheses are determined in paper 3, and the result is tested for an independent case in paper 4. Finally the difference between a planar and a 3D approach is investigated in paper 5.









CHAPTER 2

Theory

2.1. Fluid Mechanics



FIGURE 2.1. False colour picture of the turbulence structures surrounding the great red spot of Jupiter (By courtesy of NASA).

The flow in a headbox is characterized by high Reynolds numbers, defined as $Re = \frac{U_1h}{\nu}$, where U_1 is a mean flow velocity, h a typical length scale and ν the fluid kinematic viscosity. This states that the flow is of highly turbulent nature. In figure 2.1 an example of turbulent structures surrounding the great red spot (having approximately the same diameter as the Earth) of Jupiter is shown. From Newton's second law the momentum equation can be derived, i.e. it relates the fluid particle acceleration to the forces experienced by the fluid, such as surface- and body forces. For incompressible constant-property Newtonian









6 2. THEORY

fluid, the so called Navier-Stokes equation for conservation of momentum is obtained. The incompressibility of the fluid gives a divergence-free velocity field from mass conservation, i.e. $\nabla \cdot \mathbf{u} = 0$. Turbulence is characterised by random fluctuations of flow quantities, e.g. the velocity. Reynolds introduced the method of decomposition for quantities, i.e. the sum of a mean and a fluctuating parts, e.g. the instantaneous velocity $u_1 = U_1 + u'_1$. Introducing the Reynolds decomposition and averaging the Navier-Stokes equation leads to a general equation of motion expressed in mean velocity quantities for a fluid,

$$\frac{\partial}{\partial t}(\rho U_i) + \frac{\partial}{\partial x_j}(\rho U_i U_j) = \frac{\partial}{\partial x_j}(-P\delta_{ij} - \rho < u'_i u'_j > +\mu(\frac{\partial U_i}{\partial x_j} + \frac{\partial U_j}{\partial x_i})$$
 (2.1)

The difference from the instantaneous Navier-Stokes equation is the extra 'turbulent stress', $-\rho < u'_i u'_j >$, acting on the fluid called the Reynolds-stress tensor. The relations for the Reynolds stress tensor can be derived from taking moments of the Navier-Stokes equation by multiplying with the fluctuating property and averaging. This will unfortunately lead to higher-order unknown moments for the problem and illustrates the closure problem of turbulence. This means that turbulence needs to be modelled at some stage to close the set of equations. Much information is lost from the Navier-Stokes equation due to the Reynolds averaging procedure. Solving for the Navier-Stokes equation directly is one possibility, i.e. Direct Numerical Simulation (DNS). DNS is still not available for practical use for complex, high Reynolds number, 3D systems due to the vast computational effort needed, since all the scales of turbulence is needed to by resolved. One other possibility is Large Eddy Simulation(LES), which in principle resolves the large energy containing eddies and models the the smaller ones. LES has lately become more applicable to complex systems. Now the above discussion applies to single-phase fluid flow. The situation will be more complex when considering multiphase systems as for the fibre suspension for papermaking. This practically doubles the set of equations e.g. the momentum, conservation of mass and turbulence, and interaction terms will be added. A variety of such multiphase systems exists and they can be divided into single component, such as steam-water flow, or multicomponent, as air bubbles in water, fibres in air/water or slurry flows. The important thing when numerically studying such system or making measurements, is to identify the restricted volume. For example measuring the density of a gas the volume, L^3 to which instrument responds are to be larger than the molecular mean free path, λ . The ratio between the length scales is expressed by the Knudsen number, $Kn = \lambda/L$. This leads to the continuum requirement $Kn \ll 1$ for the validity of the Navier-Stokes equation. Now particles can be treated as a continuum or as discrete entities or a combination of these. A typical discrete formulation is called Langrangian, where equations for momentum transfer are set for the individual particles, e.g. Maxey & Riley (1983). A carrier fluid, continuous phase, for the Langrangian particle can be solved by using either RANS, LES or DNS to cope with the turbulence. Typically a division, with respect to interaction, is set to one-way, two-way or four-way coupling. In





"MarkoPhDThesis" — 2008/4/28 — 9:55 — page 7 — #17





2.2. FIBRE SUSPENSIONS

7

one-way coupling there is no influence on the continuous phase from the particulate phase. In two-way coupling the interaction is set both ways and in a four-way coupled system particle-particle interactions are also considered. Moreover the two components can both be treated as continuum fluids, the so-called Euler-Euler approach, e.g. Ishii (1975), Drew & Lahey (1993) and Enwald et al. (1996). For Euler-Euler modelling special attention needs to be paid to closure laws describing the interaction between the phases, i.e. the constitutive, transfer and topological laws. The constitutive law describes how the physical parameters of a phase interacts with each other; examples of flow parameters are dynamic viscosity, bulk viscosity and particle pressure. Transfer law describes the transport of mass, momentum or energy, e.q. drag force, lift force, added mass and history force. The closure problem for turbulence in two-phase modelling adds even more complexity to the modelling, since particles affect the turbulence spectrum of the continuous phase. Alternatively one can describe the multiphase system by modelling only one phase and using constitutive relations, often non-Newtonian due to the particles, i.e. for the shear stress.

2.2. Fibre Suspensions

The complexity of studying fibre suspensions experimentally stems from the opacity of the suspension which leads to obvious measurement difficulties. An example of a recent study of measurements on fibre suspensions made by ultrasound and laser techniques can be seen in work by Jäsberg (2007). The flow behaviour for higher consistencies is often of non-Newtonian nature, e.g. Gullichsen & Härkönen (1981) and Bennington et al. (1990). Furthermore a yield stress can be present, i.e. as described by a Bingham plastic fluid with shear-thinning effects for which the shear stress can be described by a Power-Law model by Oswald-de Waele, cf. Wikström & Rasmusson (2002). However, in our modelling work a dilute fibre suspension is considered. This is also the flow and concentration regime considered in the experimental investigations by Parsheh et al. (2005), Ullmar (1997), and Asplund & Norman (2004) to which our simulations are compared. Furthermore, any effect on turbulence by fibres is neglected in this study. The effect of fibres on turbulence at low consistencies is largely still unknown, although a study by Lundell et al. (2005) shows an effect of fibres on the dominant turbulent length scale for decaying turbulence for consistencies down to 0.08%. The experimental analyses by Ullmar (1997), Zhang (2001), Asplund & Norman (2004) and Parsheh et al. (2005), to which we relate our computational results in the appended papers, use fibre consistencies between 0.0001-0.01\%, which then appear to be below the limit given by Lundell et al. (2005). Kerekes & Schell (1992) introduced the Crowding factor, N, which represents the number of fibres in the volume swept out by the length of a single fibre. This indicates the level of inter-fibre contact. When the Crowding number is less than one collisions rarely occur, so this is defined as a dilute concentration. In the study by Lundell et al. (2005) the









8 2. THEORY

dominant turbulent length scale of turbulence is influenced at Crowding numbers down to 0.3 for short fibres of 0.5mm, and at N=10 for the longer 2mm fibres. Fundamental studies of the effects on fibre orientation in shear layers for laminar flows with application towards papermaking can be seen in e.g.Holm (2005) and Carlsson et al. (2007). One conclusion drawn by Carlsson et al. (2007) is that for a smooth surface most of the fibres seems to be oriented perpendicular to the flow direction at a quarter of a fibre length from the wall, while the fibres at about one fibre length from the wall were aligned with the flow direction. In this study, though, turbulent boundary layers and shear flows were considered and enhanced rotational dispersion due to turbulence is applied and discussed in later section. Since fibres follow a streamline in this study any inertial effects are neglected. To shed more light on this assumption the Stokes number, $S_t = \tau_V/\tau_F$, is analysed. The Stokes number relates the momentum response time scale of a particle, τ_V , to a characteristic timescale of the flow, τ_F . Furthermore Stokes flow is assumed and therefore the particle response time is, $\tau_V = \frac{\rho_p D}{18\mu_c}$. A fibre having a length of 3mm and thickness of 40μ m poses the question which length scale should be chosen in the response time of a fibre? The continuous phase is water at ambient conditions and the particle density is 1200 kg/m³ gives then the particle response time based on the length of the fibre to be 6.0×10^{-1} s and based on the diameter of the fibre 1.0×10^{-4} s. A characteristic time scale of the flow can be estimated from h/U_1 , where U_1 is the streamwise mean velocity and h is the height of the channel. This states that the Stokes number for the particle response time based on the fibre length varies from the inlet to the outlet of the planar contraction at the central streamline from 7.2×10^{-1} to 2.0×10^{2} , and for the response time based on fibre diameter from 1.2×10^{-4} to 3.3×10^{-2} . If the Stokes number is much lower than one the particle respond quickly to changes of the flow, while Stokes number much larger than one implies that a particle responds only very slowly to the variation of the flow. This analysis postulates that inertial effects can not be neglected if the fibre length is considered as a representative length while the opposite holds if the fibre diameter is considered. In the work of Parsheh et al. (2005) a conclusion was drawn however that the diameter of the fibre is the appropriate length scale which supports the assumption of neglecting the inertial effects also in this study. A three-dimensional approach of the fibre orientation state evolution in a turbulent accelerated flow case is considered here. Other ways can be to treat the orientation state as planar, e.g. in Advani & Tucker (1987). The fibre orientation state can also quite accurately be described by the evolution of the second-order, e.g. Parsheh et al. (2006a), or fourth-order orientation tensors, e.g. Ericsson et al. (1997). The evolution of fourth-order tensor needs closure equations for sixth-order orientation tensors etc., e.g. Advani & Tucker (1987). One main objective in e.g. Advani & Tucker (1987) is to relate the constitutive equation, i.e the bulk stress, to the orientation state, thus giving an estimate of the rheological and mechanical properties of the fluid with oriented particles.









9

2.3. FULL 3D FORMULATION OF THE FIBRE ORIENTATION MODEL

2.3. Full 3D Formulation of the Fibre Orientation Model

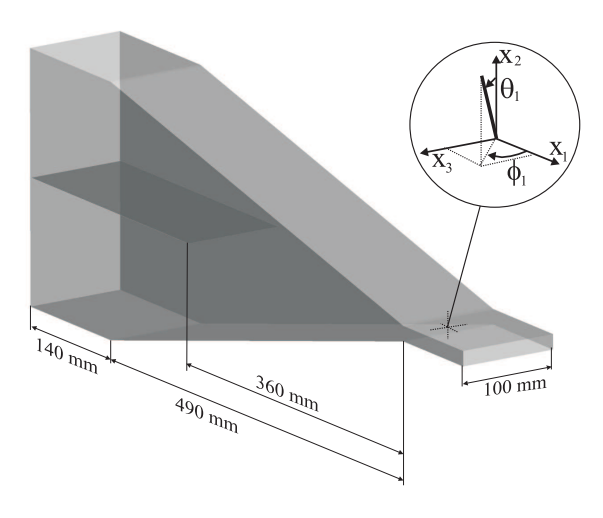


FIGURE 2.2. Schematic view of a planar contraction with definition of coordinate system and fibre orientation angles

In papers 2, 3, 4 and 5 the fully three-dimensional formulation of the fibre orientation state is solved. Here a summary of the results are presented. For a general description of the fibre orientation state we used the probability density distribution function for fibre orientation, i.e. $\Psi(x_1, x_2, \phi_1, \theta_1)$. The evolution of Ψ along the planar contraction is described by the steady-state Fokker-Planck equation, e.g. Advani & Tucker (1987) and (2.2):

$$U_{1} \frac{\partial \Psi}{\partial x_{1}} + U_{2} \frac{\partial \Psi}{\partial x_{2}} = \frac{1}{\sin \theta_{1}} \frac{\partial}{\partial \phi_{1}} \left(D_{r} \frac{1}{\sin \theta_{1}} \frac{\partial \Psi}{\partial \phi_{1}} - \sin \theta_{1} \dot{\phi_{1}} \Psi \right) + \frac{1}{\sin \theta_{1}} \frac{\partial}{\partial \theta_{1}} \left(D_{r} \sin \theta_{1} \frac{\partial \Psi}{\partial \theta_{1}} - \sin \theta_{1} \dot{\theta_{1}} \Psi \right). \tag{2.2}$$

This requires the simultaneous consideration of the azimuthal angle, ϕ_1 and the polar orientation angle, θ_1 , cf. figure 2.2. The cartesian velocity components of the average flow field are U_1 and U_2 . Rotational velocities due to the mean velocity gradients of the fibre orientational angles, ϕ_1 and θ_1 , in (2.2) are denoted, $\dot{\phi}_1$ and $\dot{\theta}_1$ respectively. In our simulation we considered a dilute fibre suspension that excludes any fibre-fibre hydrodynamic interaction. This is also the flow and concentration regime considered in the experimental works of Parsheh et al. (2005), Parsheh et al. (2006b), Ullmar (1997), Ullmar (1998) and Asplund & Norman (2004), to which our simulations are compared. The rotational diffusivity, D_r , is varied throughout the flow field at a value related to the fibre length and overall turbulent properties of the flow, as will be described in detail later. For the rotational velocities induced by the average flow field we use the fundamental study of a single undisturbed fibre by Jeffery (1922) which is applied here in the limit of an infinitely thin fibre, i.e. large









10 2. THEORY

aspect ratio. Equations for the rotational velocities of the 3D orientation vector can also be found in Goldsmith & Mason (1967), and for a large aspect ratio of the fibre these can be reduced to:

$$\dot{\phi_1} = -\sin 2\phi_1 \frac{1}{2} \frac{\partial U_1}{\partial x_1} - \sin \phi_1 \frac{\cos \theta_1}{\sin \theta_1} \frac{\partial U_1}{\partial x_2},\tag{2.3}$$

and.

$$\dot{\theta_1} = \cos\phi_1 \frac{1}{2} \left(\frac{\partial U_1}{\partial x_2} - \frac{\partial U_2}{\partial x_1} \right) + \cos\phi_1 \cos 2\theta_1 \frac{1}{2} \left(\frac{\partial U_1}{\partial x_2} + \frac{\partial U_2}{\partial x_1} \right) + \\
\sin 2\theta_1 \frac{1}{2} \left(\frac{\partial U_1}{\partial x_1} - \frac{\partial U_2}{\partial x_2} \right) + (\cos 2\phi_1 - 1) \sin 2\theta_1 \frac{1}{4} \frac{\partial U_1}{\partial x_1}.$$
(2.4)

Equations (2.3) and (2.4) are expressed in terms of mean velocity gradients applied on the centre of the fibre. The boundary conditions at $\phi_1 = 0, \pi$ are then $\frac{\partial \Psi}{\partial \phi_1} = 0$. For numerical implementation we also note that this implies zero flux conditions in the ϕ_1 -direction:

$$[D_r \frac{1}{\sin \theta_1} \frac{\partial \Psi}{\partial \phi_1} - \sin \theta_1 \dot{\phi_1} \Psi]_{\phi_1 = 0, \pi} = 0, \tag{2.5}$$

since $\dot{\phi} = 0$ at $\phi_1 = 0, \pi$. For numerical implementation of the flux in the θ_1 -direction at $\theta_1 = 0, \pi$ we note that from the definition

$$[D_r \sin \theta_1 \frac{\partial \Psi}{\partial \theta_1} - \sin \theta_1 \dot{\theta_1} \Psi]_{\theta_1 = 0, \pi} = 0, \tag{2.6}$$

i.e. the flux is zero as long as $\frac{\partial \Psi}{\partial \theta_1}$ is finite. At the centreline of the headbox contraction, in papers 2 and 3, the solution yields the result $\frac{\partial \Psi}{\partial \theta_1} = 0$ at $\theta_1 = 0, \pi$. At the inlet of the contraction we assume a homogeneous fibre orientation distribution,

$$\Psi_{x_1=0} = \frac{1}{2\pi},\tag{2.7}$$

where at all positions

$$\int_0^{\pi} \int_0^{\pi} \Psi \sin\theta_1 d\theta_1 d\phi_1 = 1. \tag{2.8}$$

2.4. Planar Formulation of the Fibre Orientation Model

An approximate approach to the study of the fibre orientation is to assume that all fibres are aligned in one plane, e.g. the $x_1 - x_3$ plane, cf. figure 2.2. Earlier modelling work that considers the evolution of the fibre orientation state as planar are, e.g. Olson & Kerekes (1998), Olson (2001), Olson et al. (2004), Parsheh et al. (2005), Parsheh et al. (2006b), Hämäläinen & Hämäläinen (2007) and Hyensjö et al. (2007). From the full 3D formulation in (2.2) the equation for









11

2.5. ROTATIONAL DISPERSION COEFFICIENT

the planar distribution function, cf. (9) in paper 5, is obtained by multiplying (2.2) with $\sin \theta_1$ and integrating over the interval $\theta_1 \in [0, \pi]$ and using (2.3):

$$U_{1} \frac{\partial \Psi_{p}}{\partial x_{1}} + U_{2} \frac{\partial \Psi_{p}}{\partial x_{2}} = \frac{\partial}{\partial \phi_{1}} \left(D_{r} \frac{\partial}{\partial \phi_{1}} \int_{0}^{\pi} \frac{\Psi}{\sin \theta_{1}} d\theta_{1} + \sin 2\phi_{1} \frac{1}{2} \frac{\partial U_{1}}{\partial x_{1}} \Psi_{p} + \sin \phi_{1} \frac{\partial U_{1}}{\partial x_{2}} \int_{0}^{\pi} \cos \theta_{1} \Psi d\theta_{1} \right). \tag{2.9}$$

In general this equation does not reduce to an equation for $\Psi_p(\phi_1)$ independent of the full 3D distribution, since two of the three terms on the right hand side cannot be expressed with Ψ_p explicitly. However, assuming that all fibres are oriented in the $x_1 - x_3$ plane, i.e. $\theta_1 = \pi/2$, it then follows that:

$$U_1 \frac{\partial \Psi_p}{\partial x_1} + U_2 \frac{\partial \Psi_p}{\partial x_2} = \frac{\partial}{\partial \phi_1} \left(D_r \frac{\partial \Psi_p}{\partial \phi_1} + \sin 2\phi_1 \frac{1}{2} \frac{\partial U_1}{\partial x_1} \Psi_p \right). \tag{2.10}$$

Note that the mean shear velocity, $\frac{\partial U_1}{\partial x_2}$, for the advection term in fibre orientation space, see $\dot{\phi}_1$, has no effect on (2.10). This formulation has earlier been used by Olson & Kerekes (1998), Olson (2001), Olson et al. (2004), Parsheh et al. (2005), Parsheh et al. (2006b) and Hyensjö et al. (2007). Hämäläinen & Hämäläinen (2007) and Niskanen et al. (2008) also included a translational term. We emphasize that (2.10) is strictly valid only if all fibres are oriented in the x_1-x_3 plane. In the more general case (2.9) does not reduce to the planar equation (2.10). Thus large deviations from the 3D case may be expected in e.g. boundary layers where the fibres are not mainly oriented in the x_1-x_3 plane. We consider the interval $\phi_1 \in [0,\pi]$ for the planar formulation . The boundary conditions at $\phi_1=0,\pi$ are then $\frac{\partial \Psi}{\partial \phi_1}=0$. For numerical implementation we also note that this implies zero-flux conditions in the ϕ_1 -direction:

$$[D_r \frac{1}{\sin \theta_1} \frac{\partial \Psi}{\partial \phi_1} - \sin \theta_1 \dot{\phi}_1 \Psi]_{\phi_1 = 0, \pi} = 0, \tag{2.11}$$

since $\dot{\phi} = 0$ at $\phi_1 = 0, \pi$. At the inlet of the contraction we assume a homogeneous fibre orientation distribution,

$$\Psi_{x_1=0} = \frac{1}{\pi},\tag{2.12}$$

where at all positions

$$\int_0^{\pi} \Psi_p d\phi_1 = 1. (2.13)$$

2.5. Rotational Dispersion Coefficient

The rotational diffusivity coefficient, D_r , can be considered analogous to Brownian motion where a small particle exhibits a random motion due to collisions of molecules with the particle. The infinitesimally small fibres are affected by the local turbulent fluctuations hence dispersing the fibre orientation distribution function in (2.2). In paper 1 the rotational diffusivity coefficient, D_r , is determined by a method based on the inverse of the Kolomogorov time scale, τ_{η}









12 2. THEORY

in (2.16). This will be denoted Hypothesis III in the following papers 3, 4 and 5. In paper 1 the constant of proportionality was determined with an ad hoc level of turbulence entering the planar contraction. In paper 2, two different hypotheses, denoted Hypotheses I and II, were presented for the variation of the non-dimensional rotational diffusivity with non-dimensional fibre length, L_f/η , and Reynolds number based on the Taylor micro-scale of the turbulence, Re_{λ} . To describe the relations between D_r and k and ϵ we follow the notation by Shin & Koch (2005) who express D_r in terms of the fibre orientation auto-correlation integral time, T_p as

$$D_r = \frac{1}{2T_p},\tag{2.14}$$

where T_p is expressed in terms of two different scalings

$$T_p = \tau_{\eta} f_{\eta}(Re_{\lambda}, L_f/\eta) = \tau_{\Lambda} f_{\Lambda}(Re_{\lambda}, L_f/\Lambda). \tag{2.15}$$

The first one is associated with the Kolmogorov time scale

$$\tau_{\eta} = (\frac{\nu}{\epsilon})^{\frac{1}{2}},\tag{2.16}$$

and the second one with the Eulerian integral time scale

$$\tau_{\Lambda} = \frac{\Lambda}{u_{rms}},\tag{2.17}$$

where $u_{rms} = \sqrt{\frac{2k_0}{3}}$. The non-dimensional functions f_{η} and f_{Λ} are generally dependent on the Reynolds number based on the Taylor micro-scale, $\lambda = \sqrt{15}u_{rms}\sqrt{\nu/\epsilon_0}$,

$$Re_{\lambda} = \frac{u_{rms}\lambda}{\nu},$$
 (2.18)

and the non-dimensional fibre lengths $L_f/\eta,\,L_f/\Lambda$ scaled with the Kolmogorov length scale

$$\eta = (\nu^3/\epsilon)^{1/4},\tag{2.19}$$

and the turbulent Eulerian integral length scale, Λ , respectively. We will assume here that Λ is of the same order magnitude as the large energy bearing eddies in turbulence, given by

$$\Lambda \approx L \equiv \frac{k_0^{\frac{3}{2}}}{\epsilon_0}.\tag{2.20}$$

The DNS results from Shin & Koch (2005) describing the fibre orientation auto-correlation time, T_p , as a function of fibre length, is shown in figure 2.3 in two different non-dimensional units. In figure 2.3 (a) the Kolmogorov time and length scales are used for non-dimensionalization, whereas in figure 2.3 (b) the Eulerian integral time and length scales are used. Shin & Koch (2005) draw the conclusion that neither Kolmogorov scales or Eulerian integral scales collapse the data independently of the Reynolds number, Re_{λ} . They specifically note that whereas the Eulerian integral time, τ_{Λ_1} , is actually similar in magnitude









13

2.5. ROTATIONAL DISPERSION COEFFICIENT

to T_p , the Kolmogorov time scale, τ_{η} , is substantially smaller. Figure 2.3(b) also shows the quadratic asymptotes for short fibres fitted by Shin & Koch (2005) according to:

$$\frac{T_p}{\tau_{\Lambda_1}} = b_{p,0} + b_{p,2} (\frac{L_f}{\Lambda_1})^2, \tag{2.21}$$

The coefficients $b_{p,0}$ and $b_{p,2}$ are indeed dependent on Re_{λ} where the trend is

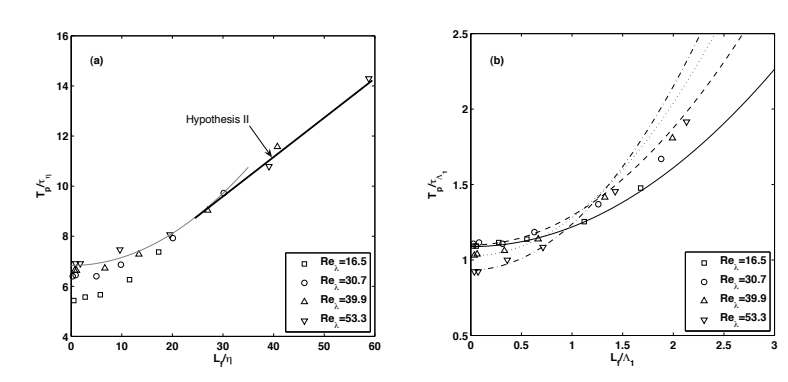


FIGURE 2.3. DNS data for various Re_{λ} by Shin & Koch (2005) of the integral time for fibre orientation as a function of fibre length with respect to Kolmogorov time and length scales in (a), and Eulerian integral time and length scales in (b). Quadratic asymptotes in (b) of the DNS data according to (2.21)

that $b_{p,0}$ decreases and $b_{p,2}$ increases with Re_{λ} . Based on the three-dimensional energy spectrum of the DNS generated homogeneous isotropic turbulent flow by S&K, the Eulerian integral length scale, Λ_1 , in (2.21) and figure 2.3 (b), is defined as the two-point velocity correlation in the longitudinal direction, i.e. x_1 -direction. (Note that in the present work the Eulerian integral length scale is defined by (19) in paper 2). In all, Shin & Koch (2005) conclude that their expectation, that T_p/τ_η is a function, f_η , only of L_f/η , would be possible only at very high Re_{λ} and with large values of f_η . Guided by the data of figure 2.3 (a,b), we present two hypotheses for T_p . The first hypothesis is based on the quadratic asymptotes for short fibres using the Eulerian integral scaling. In a first approximation, for very small values of L_f/Λ_1 , the second term of (2.21) can be neglected, which according to figure 2.3 (b) seems reasonable at least for, say, $L_f/\Lambda_1 < 0.3$. The remaining coefficient, $b_{p,0}$, is still dependent on Re_{λ} and we make the assumption

$$f_{\Lambda}^{I} = \frac{T_{P}^{I}}{\tau_{\Lambda}} = \frac{1}{(a_1 + b_1 Re_{\lambda})},$$
 (2.22)

where a_1 and b_1 are constants independent of L_f/Λ . The second hypothesis for T_p considers long fibres in terms of the Kolmogorov scaling and in the









14 2. THEORY

limit of large Re_{λ} . From figure 2.3 (a) we observe that for $L_f/\eta > 25$, and data of Reynolds numbers in the interval $30 < Re_{\lambda} < 50$, the dependence on Re_{λ} is much weaker and the data collapse approximately on a straight line, as indicated. Our simulations are in the range of $Re_{\lambda} = 50 - 250$. Thus we assume

$$f_{\eta}^{II} = \frac{T_P^{II}}{\tau_{\eta}} = a_2 + b_2 \frac{L_f}{\eta}, \tag{2.23}$$

where a_2 and b_2 are constants independent of Re_{λ} . As commented by Shin & Koch (2005), f_{η} may be expected to be independent of $Re_{\lambda} \gg 1$ as the largest velocity gradients occur in Kolmogorov eddies, although their DNS-results do indicate an overall Re_{λ} -dependence. As a complementary part of the second hypothesis for smaller values of L_f/η , one may consider a quadratic asymptote that joins smoothly with (2.23)) at $L_f/\eta=25$. This is also indicated in figure 2.3 (a), and would represent the limit for large Re_{λ} . The hypotheses for (2.15) were given for, Hypothesis I in (2.22)¹ and Hypothesis II in (2.23), and this is further presented and summarized in table 2.1 for the planar formulation and in 2.2 for the full 3D formulation. The different optimisation strategies, Opti1 and Opti2, are characterised by how experimental results are weighted for determining the parameters for the respective hypotheses. Parameter values for Opti3 is determined in the study of paper 2 and was solely made for the full 3D formulation, cf. table 2.2.

Table 2.1. Summary of the hypotheses and parameters for the planar formulation of the fibre orientation model

	D_r	Opti1	Opti2
Hypothesis I	$\frac{1}{2\tau_n} \frac{2\sqrt{10}}{3} \frac{(a_1 + b_1 Re_{\lambda})}{Re_{\lambda}}$	$a_1 = 0.51$	$a_1 = 0.06$
	,	$b_1 = 0.0046$	$b_1 = 0.0062$
Hypothesis II	$\frac{1}{2\tau_{\eta}} \frac{1}{a_2 + b_2 \frac{L_f}{\eta}}$	$a_2 = 13.17$	$a_2 = 58.3$
	,	$b_2 = 1.01$	$b_2 = 0.166$
Hypothesis III	$\frac{1}{2\tau_{\eta}}C_1$	$C_1 = 0.0082$	$C_1 = 0.0076$





 $^{^{1}}$ See paper 2 (27) or table 2.2 for (2.22) expressed in the Kolmogorov timescale

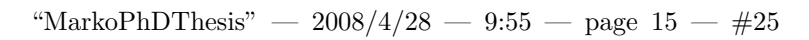






Table 2.2. Summary of the hypotheses and parameters for the full 3D formulation

	D_r	Opti1	Opti2	Opti3
Hypothesis I	$\frac{1}{2\tau_{\eta}} \frac{2\sqrt{10}}{3} \frac{(a_1 + b_1 Re_{\lambda})}{Re_{\lambda}}$	$a_1 = 0.435$	$a_1 = 0.033$	$a_1 = 0.0473$
	,,	$b_1 = 0.0049$	$b_1 = 0.00703$	$b_1 = 0.0052$
Hypothesis II	$\frac{1}{2\tau_{\eta}} \frac{1}{a_2 + b_2 \frac{L_f}{\eta}}$	$a_2 = 22.85$	$a_2 = 61.5$	$a_2 = 68.23$
	,	$b_2 = 0.84$	$b_2 = 0.089$	$b_2 = 0.3525$
Hypothesis III	$\frac{1}{2\tau_n}C_1$	$C_1 = 0.00835$	$C_1 = 0.0078$	$C_1 = 0.0055$









CHAPTER 3

Purpose and Methods

In the work related to the appended papers 1, 2, 3, 4 and 5, a commercial Computational Fluid Dynamics (CFD) code Ansys CFX 11.0 is used for solving eg. (2.1). For handling the turbulence a second-order closure is applied, called the ω -Reynolds Stress model. This means that the transport equation of the Reynolds-stresses is solved with approximations for closing the set of equations, e.g. higher order moments, pressure correction, dissipation etc. Solving for contracting turbulent flows, the mean strain field is changed and therefore also the state of the turbulent anisotropy, which needs to be considered. Thus, the use of an isotropic turbulence model, based on the Boussinesq hypothesis (e.g. $K - \epsilon$ model), is not applicable. This is related to the fact that the Boussinesq hypothesis assumes that the components of the Reynolds Stress tensor are proportional to the mean strain field, and that the turbulence and mean flow are in equilibrium. Therefore, the turbulence in this study uses a second-moment closure, e.g. the ω -Reynolds Stress Model provided with default parameters specified in the CFD-code. Different turbulence models were studied by Parsheh (2001) in a planar contracting flow, and the isotropic $k-\varepsilon$ turbulence model failed to describe the turbulence quantities in a planar contraction, while the LLR-Reynolds Stress Model and Algebraic Reynolds Stress models perform better. The spatial discretisation of the partial differential equations were mainly made by hexahedral elements throughout this work. The partial differential equations (2.2) and (2.10) were solved with Comsol Multiphysics 3.3. The mesh of the discrete finite elements was optimised for a mesh independent solution of (2.2) and (2.10).

3.1. Paper 1

The main purpose of paper 1 was to study the the effect of turbulence generating vanes, and their location in a planar contraction, on fibre orientation anisotropy using the planar approach to the evolution of the fibre orientation state. In paper 1 the constant of proportionality for the the rotational diffusivity coefficient, D_r , was determined with an ad hoc level of turbulence entering the planar contraction. Qualitative comparison was made with experimental results in the literature. The geometry consists of a planar contraction with one vane in the centreline of the contraction. Two of the four different vane tips in the work by Parsheh (2001) has been studied here, i.e. the blunt and the tapered one. The planar contraction is solved with symmetry planes in the









3.2. PAPER 2 17

plane of contraction. The Reynolds number based on the inlet height of the contraction and the inlet mean velocity is in order of 50000. The turbulence quantities at the inlet were set to a specified turbulence intensity, $TI = u_{rms}/U$, of 3.7%. The TI value is an estimate from measurements by Parsheh (2001). The ω -Reynolds Stress Model was used for the turbulence purpose. The outlet boundary conditions were set to a opening with zero relative pressure gradient specified.

3.2. Paper 2

In paper 2 the fully 3D formulation of the fibre orientation state is solved. Two new hypotheses for the non-dimensional rotational diffusivity are presented, each based on two different turbulent time scales, i.e. the Kolmogorov time scales and the time scale associated with large energy bearing eddies. The experiments considered for comparison with the simulations are two cases from Parsheh et al. (2005), i.e. Cases 1 and 2, and two cases described in a study by Ullmar (1997), i.e. Cases 3 and 4. The properties that we need to identify at the inlet for each case are streamwise mean velocity, $U_{1,0}$, turbulent kinetic energy, k_0 , and turbulent dissipation rate, ϵ_0 . The first study, Cases 1 and 2, describes a mesh-generated turbulence that changes by means of increasing the flow rate, i.e. $Re = 85 \times 10^3$ and $Re = 170 \times 10^3$. In Cases 3 and 4, the turbulence is generated by a bundle of pipes, i.e. 3 x 7 pipes, with a round-to-round sudden pipe expansion followed by a round-to-square step, leading to a square shaped outlet, entering a short straight channel before the contraction. For Case1 the level of kinetic energy of turbulence, k_0 , is estimated with an approximation of decaying isotropic turbulence, from a uniform grid in a straight channel, given by Roach (1987) together with the experimental data provided by Parsheh et al. (2005) to be:

$$k_0 = \frac{3}{2}U_0^2 (1.2(\frac{l}{d})^{-\frac{5}{7}})^2, \tag{3.1}$$

where 1.2 is a constant based on grid geometry and has been fitted to the experimental result for Case1, 1 is the downstream position from the grid, d is the grid bar width of the mesh, and U_0 is the streamwise velocity upstream of the contraction. Based on the equation for the mean kinetic energy of turbulence, and the assumption of decaying isotropic turbulence, *i.e.* there is no production of turbulence and the mean flow is constant, the dissipation rate of turbulent energy at the inlet of the contraction, ϵ_0 , can be estimated, for Case 1 and Case 2, together with (3.1) from:

$$U\frac{\partial k_0}{\partial x_1} = -\epsilon_0. (3.2)$$

The estimation of turbulence levels for, Case3 and Case4, *i.e.* Ullmar (1997) and Ullmar (1998), has been made with CFD modelling. Mean quantities of k and ϵ from simulations just before the contraction were used for evaluation of the inlet value.









18 3. PURPOSE AND METHODS

3.3. Paper 3

The purpose of paper 3 was to determine the value of the rotational dispersion coefficient of stiff fibres in an anisotropic turbulent fluid flow. The difference with paper 2 is that the level of the rotational diffusivity, which is now considered locally dependent, will be determined with an optimization of the parameters for three different hypotheses, i.e the one in paper 1 and the two new ones in paper 2. The inlet values for the turbulent quantities, k_0 and ϵ_0 , for Case

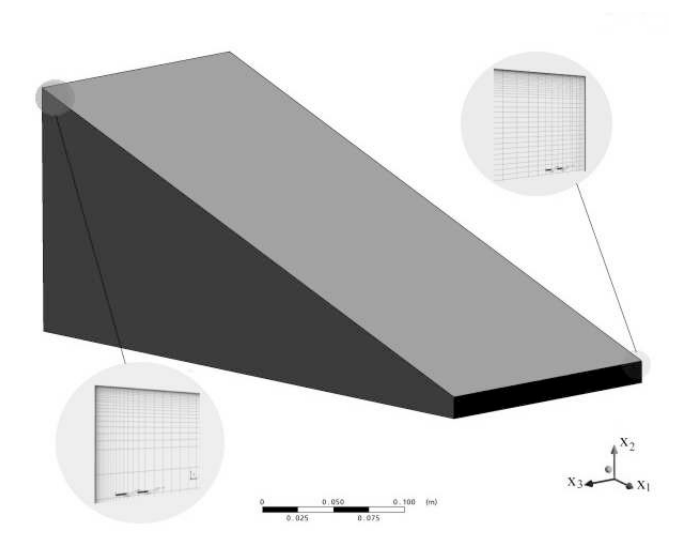


FIGURE 3.1. Outline of the 3D CFD model of the contraction and an example of the mesh at two positions, Case1 and Case2.

1 and Case 2 are set from (3.1) and (3.2) at a position where the contraction starts. Whereafter the full 3D CFD simulation is carried out for Case 1 and Case 2, cf. figure 3.1. For Cases 3 and 4 the average outlet values of U_0 , k_0 and ϵ_0 from the model in figure 3.2 gave the inlet values for the planar contraction model. The contraction CFD-model consists of a contraction and a straight channel with the same height as the contraction outlet height, cf. figure 3.3.

3.4. Paper 4 and Paper 5

In paper 4 the result from paper 3 is considered and is evaluated against an independent experimental case. In paper 5 the differences between the fully 3D orientation formulation of the fibre orientation model in (2.2) and the planar one in (2.10) are studied. The CFD model in papers 4 and 5 considers the geometry in the experimental work by Asplund & Norman (2004), cf. figure 3.4. It consists of a tube bundle with one axisymetrical step followed by a round-to-squared step after entering a straight channel part just before the planar contraction which has its exit in a straight channel. The measurement of the









3.4. PAPER 4 AND PAPER 5 19

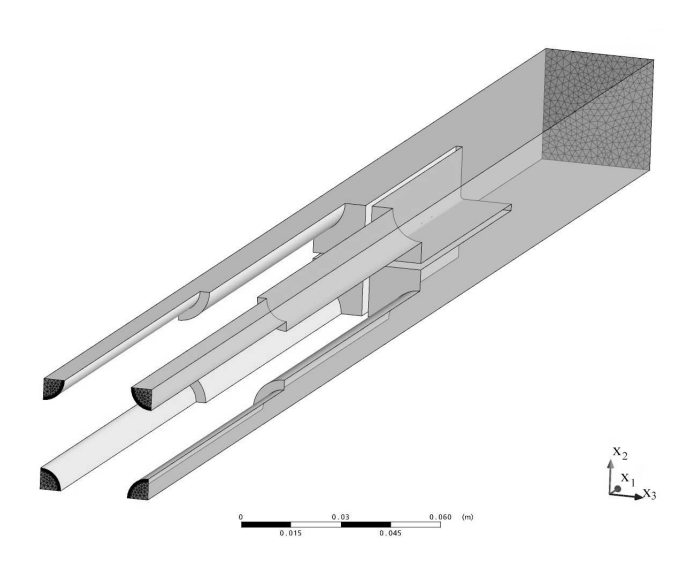


FIGURE 3.2. Outline of the 3D CFD-model of the symmetrical tube bundle and the straight channel.



FIGURE 3.3. Outline of the 3D CFD model of the contraction with the outlet straight channel.

fibre orientation state was made in this final straight channel part, cf. Asplund & Norman (2004) and figure 3.4. In the contraction a central guiding vane was inserted having five different lengths relative to the outlet of the contraction, i.e denoted here as Case A-E. The blunt vane tip with a thickness of 0.2mm was









20 3. PURPOSE AND METHODS

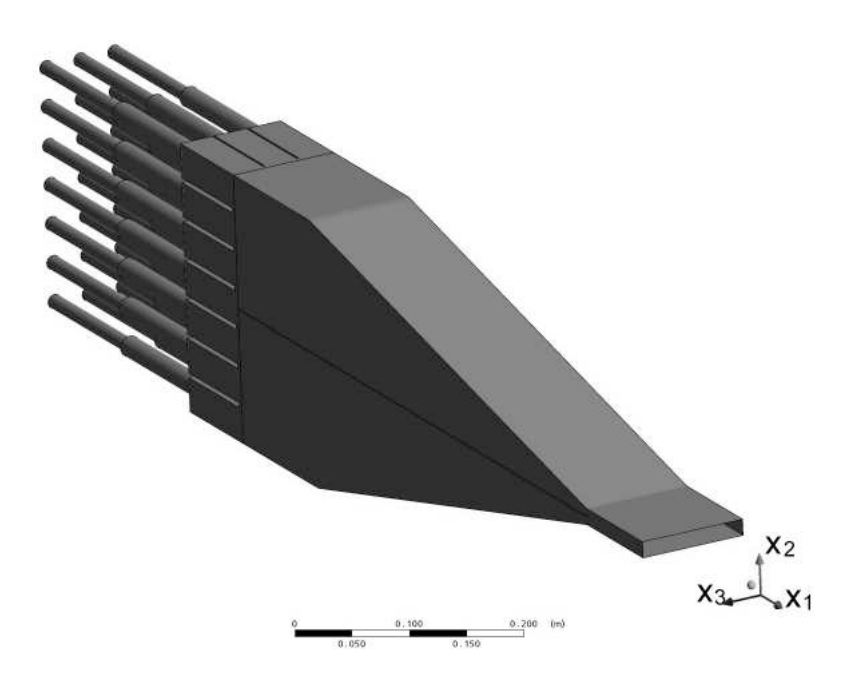


FIGURE 3.4. Outline of the 3D CFD model

positioned relative to contracting outlet at; 0 mm (CaseA), -30 mm (CaseB), -60 mm (CaseC), -120 mm (CaseD) and -360 mm (CaseE) respectively. The length of the straight channel is 140 mm and the contraction length is 490mm, cf. view of the model for Case E in figure 2.2. The CFD result was simulated obtained for a steady-state solution using 6.0×10^6 hexahedral elements. The inlet boundary conditions was taken to be, a turbulence intensity of 3.7% and a dissipative length scale of $0.3D_{in} = 0.3 \times 13 \times 10^{-3} \text{m} = 3.9 \times 10^{-3} \text{m}$, were specified at the inlet tube $(D_{in} = 13 \times 10^{-3} \text{m})$, i.e. to the left in figure 3.4. An analysis was made, not presented here, determining that the choice of this inlet turbulence level $(1.48 \times 10^{-2} \text{ m}^2/\text{s}^2)$ is not sensitive due to the large amount of turbulent energy generated in the first step and a strong dampening of the turbulence in the relatively small tube.









CHAPTER 4

Results

In this section some of the results of papers 1, 2, 3, 4 and 5 are highlighted and summarized. The rotational Peclet number defined here as $\text{Pe}_{\text{r}} = \frac{\partial U_1}{\partial x_1}/D_r$ increases rapidly along the contraction, see figure 4.1, whereby the diffusivity has its major role at the beginning of the contraction. Clearly, a higher turbulence level at the inlet of the contraction also decreases the value of the rotational Peclet number, i.e Case 1 is less influenced by the turbulence than Case 4. According to the work by Parsheh *et al.* (2005) the effect of turbulence becomes insignificant when $\text{Pe}_{\text{r}} > 10$, which corresponds to approximately the last 25% of the total contraction length, *cf.* figure 4.1.

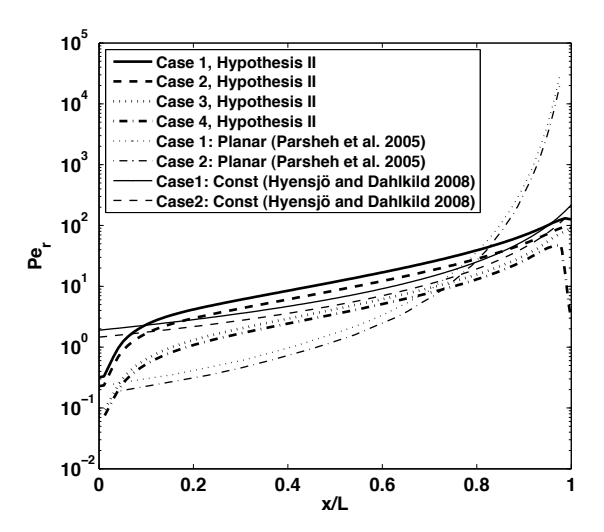


FIGURE 4.1. The variation of Pe_r , using Hypothesis II, along the central steamline of the contraction for the different flow Cases 1 to 4, related to the normalized contraction length. Also Pe_r from the work by Parsheh *et al.* (2005)

In our simulation the Peclet number of 10 occurs around x/L=0.5 considering both Cases 1 and 2. Figure 4.1 also clearly demonstrates the main characteristic









difference in behaviour between our dispersion coefficient and that of Parsheh $et\ al.\ (2005),\ cf.$ Cases 1 and 2. The variation of the dispersion coefficient defined by Parsheh $et\ al.\ (2005)$ is based qualitatively on the overall decrease of the turbulence intensity in the flow while our model in Hypothesis II of paper 3, 4 and 5 considers a time and length scale associated with the local turbulent flow properties and a fibre-length ratio. Furthermore the levels of the dispersion coefficients are not directly comparable since our approach considers the fully three-dimensional fibre orientation state and the work by Parsheh $et\ al.\ (2005)$ regards the orientation state as planar. In figure 4.1 Per for a constant D_r from paper 2 is also shown. As can be seen and expected the level is of the same order as the result in paper 3 using local turbulent flow properties for evaluation of D_r .

To test the first hypothesis, discussed in the previous paragraph, we plot $2D_r\tau_{\Lambda}=\tau_{\Lambda}/T_p$ versus Re_{λ} for the simulation results in figure 4.2. The corresponding linear regression line, according to (2.22), with the parameters, $a_1=0.047$ and $b_1=0.0052$ is also shown. The good match illustrates that for the limits of small L_f/Λ , D_r scales in magnitude with the inverse of the Eulerian integral time scale and $D_r\tau_{\Lambda}$ increases with Re_{λ} . This trend is also obtained by Shin & Koch (2005) in their simulations, cf. figure 2.3(b). Their values of $1/b_{p,0}$, cf. eq. (2.21), are also shown in figure 4.2, including a corresponding linear regression line for their data and for the larger Reynolds numbers. Also in figure 4.2, a special case of a linear regression line drawn through the origin is shown. Considering the values of L_f/η in the studied cases

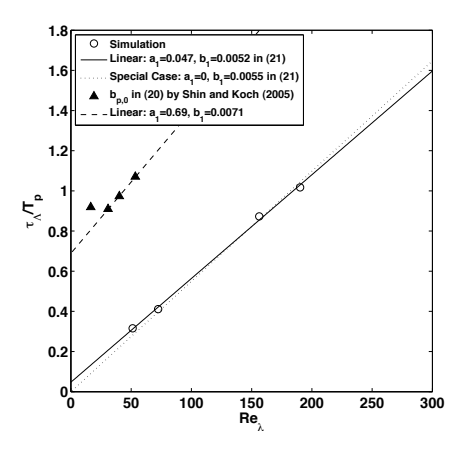


FIGURE 4.2. Determined parameters related with the inverse of (2.22), showing the Eulerian integral time scale, τ_{Λ} , related to the fibre orientation integral time scale, T_p , as a function of Re_{λ}

1-4, we have, $25 \lesssim L_f/\eta \lesssim 60$ and $50 < Re_{\lambda} < 200$. This is well above the lower limits for L_f/η and Re_{λ} which determine when T_p/τ_{η} may be regarded as









23

independent of Re_{λ} and linear in L_f/η according to the simulations by Shin & Koch (2005), cf. figure 2.3(a). Considering the second hypothesis in (2.23), the simulated results with corresponding linear regression line are shown in figure 4.3. The parameters determined are $a_2=68.2$ and $b_2=0.352$, which gives a good fit. The relative slope, $\frac{1}{f_{\eta}}\frac{d}{d(L_f/\eta)}(f_{\eta})$, at $L_f/\eta=25$ is of the same order of magnitude as that found in the results of Shin & Koch (2005), although the values of T_p^{II}/τ_{η} are larger by a factor of 10. The complementary part of the second hypothesis for $L_f/\eta<25$ and large Re_{λ} is also given in figure 4.3 as the quadratic asymptote that joins smoothly with (2.23) at $L_f/\eta=25$.

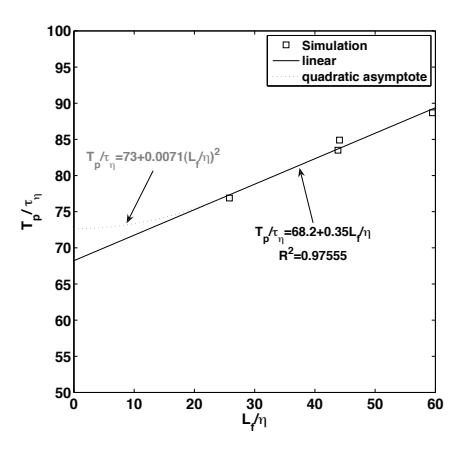


FIGURE 4.3. Optimized parameters, a_2 and b_2 , according to (2.23) showing the fibre orientation integral time scale, T_p , related to the Kolmogorov time scale, τ_{η} , as a function of L_f/η , and the complementary quadratic asymptote for $L_f/\eta < 25$

Previous studies show that the dispersion level will decrease as the fibre length is increased, e.g. in Olson & Kerekes (1998), Olson (2001) and Shin & Koch (2005). As shown in figure 4.4, a similar trend for Hypothesis II is achieved at the measuring position after the contraction for Case 3. In figure 4.4, the planar profiles for respective orientation angles are shown, i.e. the plane $\theta_1 = \pi/2$ in (a) and the plane $\phi_1 = 0$ in (b). The corresponding 3D probability distribution function is evaluated in figure 4.10 for a fibre length of 3mm. The evaluation in figure 4.4 is made by averaging over all possible complementary angles in the considered plane.

The five different experimental cases provided by Asplund & Norman (2004) of the contraction outlet profiles across the jet from centreline ($x_2 = 0mm$ mm) to upper boundary layer wall ($x_2 = 7.5$ mm), are shown in figure 4.5. The difference between each case is characterized by the length of the dividing vane in the middle of the planar contraction, *i.e.* the vane tip ends at different positions relative to the outlet of the contraction. Three different characteristic









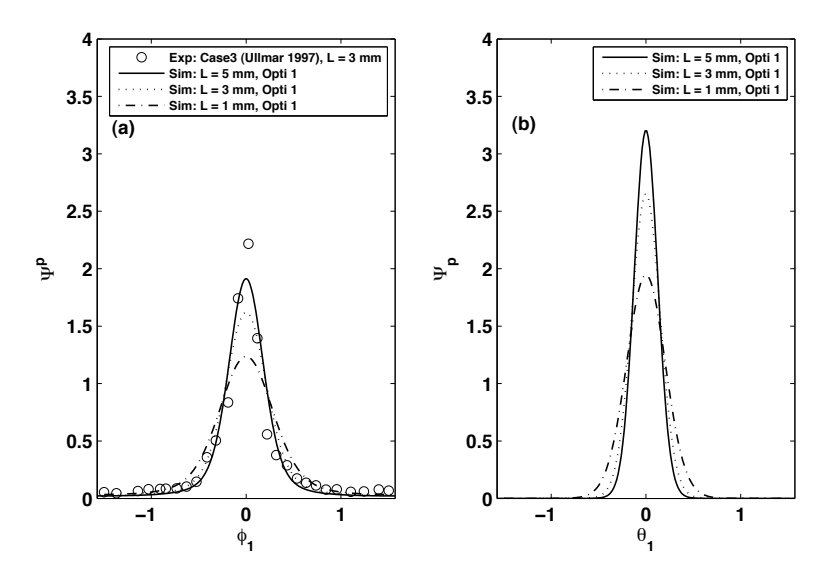


FIGURE 4.4. Effect of fibre length, with Hypothesis II and Opti3 parameters, on the planar fibre orientation distribution for ϕ_1 in (a) and θ_1 in (b) for Case 3, experimental data provided by Ullmar (1997)

regions can be distinguished in figure 4.5; the upper boundary layer, the undisturbed flow and the wake. As can be seen in figure 4.5 the upper boundary layer disperses the orientation state to almost the same level for all the cases. The general trend for the wake region is that the fibre orientation anisotropy decreases the closer the vane tip is to the outlet, cf. figure 4.5. Note, however, that there is a large spread in the experimental results. In figure 4.6 the planar and 3D approaches are compared to the experimental Case A using hypothesis II for the rotational diffusivity. The 3D approach gives the same level of anisotropy for the boundary layer as the experimental result while the planar approach shows a result far more from the experiments. For Opti1 and planar approach the result goes below the isotropic state at $A_{\phi_1} = 1$, which states that the fibres are more oriented in the x_3 than in x_1 direction, cf. figures 4.6. In the wake region the 3D approach gives slightly larger anisotropic values than the planar one. In figure 4.7 some fluid properties at three different positions, (a) and (b), 70 mm upstream, (c) and (d), 30 mm downstream, (e) and (f), 180 mm downstream the vane tip, are shown. Figure 4.7, (a) and (b), illustrates the boundary layer in the vicinity of the vane wall with the normalized velocity profile in (a) and some normalized turbulent quantities in (b). The Reynolds shear stress, $-\langle uv \rangle$, has its maximum close to the wall and drops to zero at the wall so that the wall stress consists solely of the viscous part. Figure 4.7, (c), illustrates the velocity defect in the wake since the upstream vane









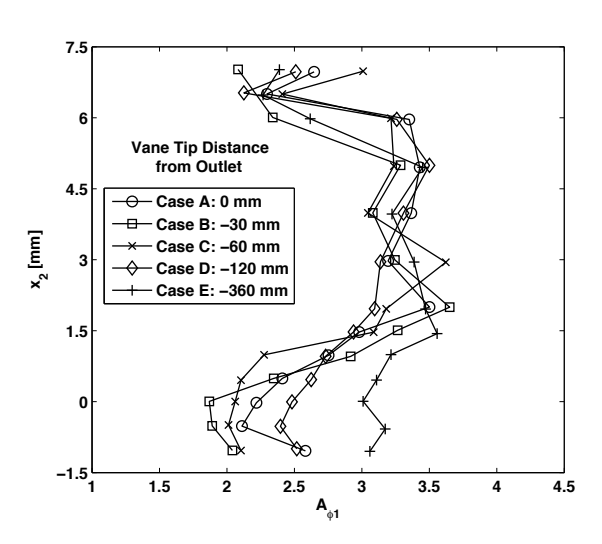


FIGURE 4.5. Experimental results of the fibre anisotropy across the jet for the five cases A-E, by Asplund & Norman (2004)

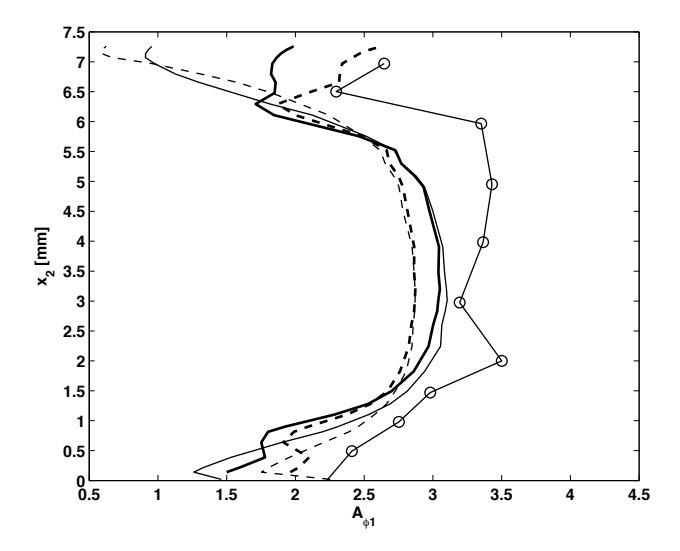


FIGURE 4.6. Experimental (o), by Asplund & Norman (2004), and present simulated results of the fibre orientation anisotropy profiles, planar(normal) and 3D(bold), for the different optimization approaches, Opti1(dashed), Opti2 (line), for Hypothesis II and Case A.





"MarkoPhDThesis" — 2008/4/28 — 9:55 — page 26 — #36





4. RESULTS

tip has a thickness of t=0.2 mm. In figure 4.7 (d) the corresponding normalized turbulent quantities are shown. Since the second-order closure turbulence model allows redistribution among components of the Reynolds stress, the basic modelling tool for predicting the wake is present, although there is a lack of experimental validation. Finally in figure 4.7, (e) and (f), the normalized velocity and normalized turbulent quantities are displayed at the evaluation position of the fibre orientation anisotropy profiles. The upper wall at this position is at $x_2 = 7.5$. At the position of 4.7 (e) and (f), the boundary layer in the straight part after the contraction is growing and is far from being fully developed. The velocity defect of the wake is quite weak here and is not visible in the graph of figure 4.7 (e). In figure 4.8 the effect of vane position is compared between the two approaches, planar and 3D. Comparing figure 4.8 with figure 4.5 we see that not only the boundary layers but also the wake region are better captured with the 3D approach. The 3D probability distributions for the specific regions, i.e. the boundary layer, undisturbed region and the wake, are illustrated in figures 4.9, 4.10 and 4.11. It is notable that in figure 4.9, the local mean value of the fibres' orientation in θ_1 is more than $\pi/2$, indicating that the fibres have a preferred orientation that is higher than the upper wall, cf. figure 2.2. The vice versa trend can be seen in the wake region, cf. 4.11. In the work by Hyensjö et al. (2007) this trend qualitatively follows the principal strain-rate axis of the flow field. Furthermore, as can be seen in figure 4.10, the undisturbed region has the highest peak values, which is reflected in higher fibre orientation anisotropy values. Note that any fibre interaction with the wall is excluded which allows the numerical simulations of the fibre orientations to get closer to the wall than expected with the real fibres in the experiments.









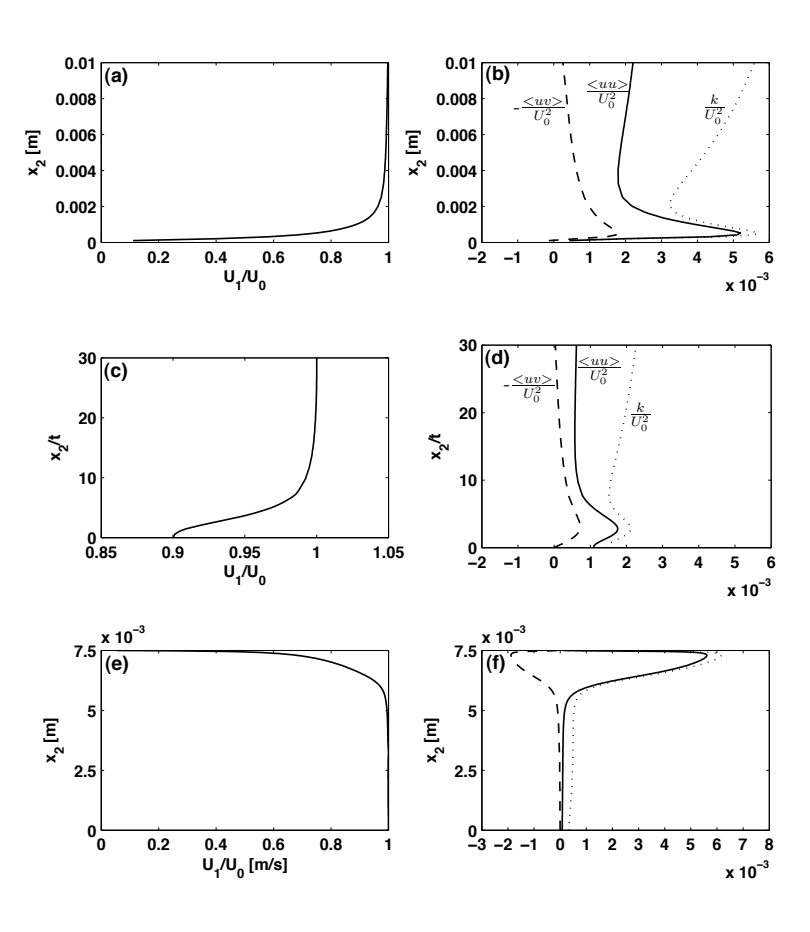


FIGURE 4.7. Result of the flow for CaseD; (a) the normalized streamwise mean velocity, U_1/U_0 , profile at 70mm upstream the vane tip, (b) corresponding normalized mean turbulence properties, (c) normalized streamwise mean velocity, U_1/U_0 , profile 30mm downstream the vane tip in the wake with corresponding turbulence properties in (d), (e) normalized streamwise mean velocity, U_1/U_0 , profile 180mm downstream the vane tip at the measurement position with corresponding mean turbulent quantities, $< uu > /U_0^2$ (solid), $- < uv > /U_0^2$ (dashed) and turbulent kinetic energy k/U_0^2 (dotted) in (f).









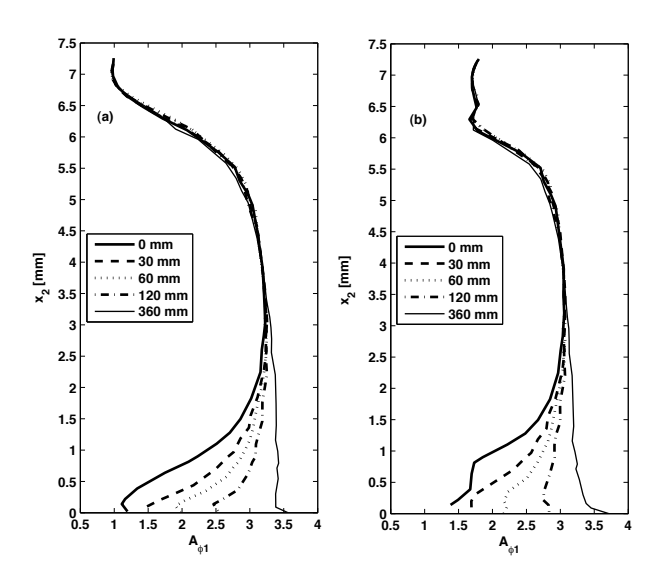


FIGURE 4.8. Effect of vane position on fibre orientation anisotropy, simulated results for Case A-E, with Opti2 and Hypothesis I, planar(a) and 3D(b) approach.

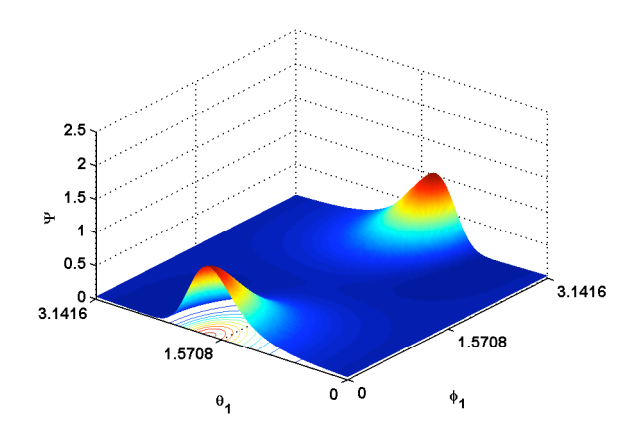


FIGURE 4.9. 3D probability density distribution function of the fibre orientation in the boundary layer close to the wall (y=6.3mm), Case A, Opti2 and Hypothesis II.









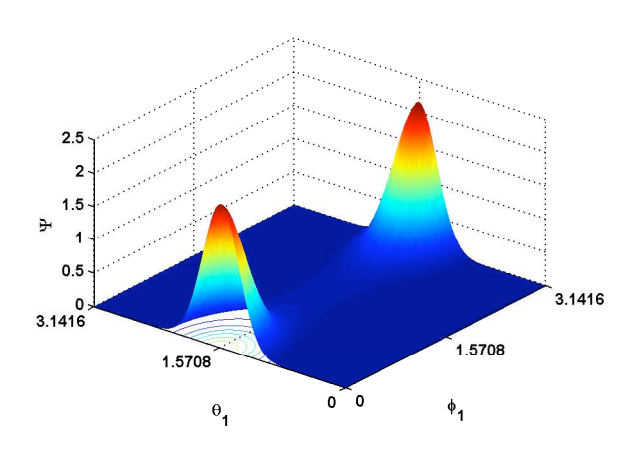


FIGURE 4.10. 3D probability density distribution function of the fibre orientation at the undisturbed region(y=4mm), Case A, Opti2 and Hypothesis II.

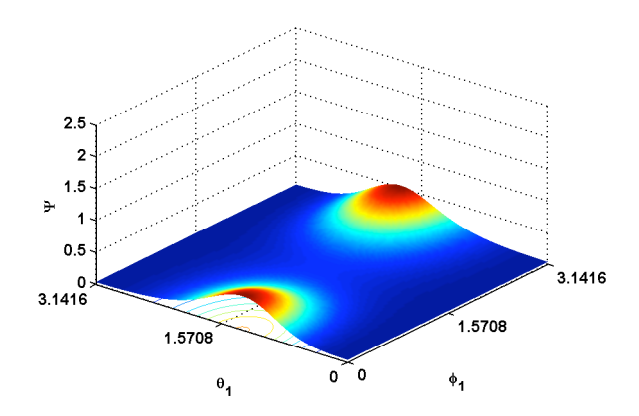


FIGURE 4.11. 3D probability density distribution function of the fibre orientation in the wake(y=0.2mm), Case A, Opti2 and Hypothesis II.









CHAPTER 5

Concluding Remarks

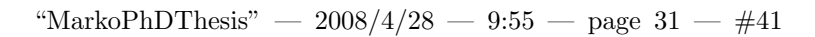
By means of solving the evolution of a convective-dispersion equation, i.e. the Fokker-Planck equation, a fully 3D approach with respect to the position and the two fibre angles, polar and azimuthal angles, following a streamline is presented, cf. (2.2). As an input to the fibre orientation model the turbulent flow field is solved by Computational Fluid Dynamics (CFD) with second-order closure of the turbulence model. In this work two new hypotheses have been presented for the variation of the non-dimensional rotational diffusivity with non-dimensional fibre length, L_f/η , and Reynolds number based on the Taylor micro-scale of the turbulence, Re_{λ} , denoted Hypotheses II and I respectively. The optimization of parameters for the different hypotheses correlated against a central streamline in Hyensjö et al. (2008), paper 3, showed a good agreement with the experimental results, conducted by Asplund & Norman (2004), in the undisturbed region. However there is a lack of experimental data to make a fully satisfactory optimization from a mathematical point of view, cf. Hyensjö et al. (2008), paper 3. Moreover, it is particularly interesting that the boundary layer region and the wake region are predicted fairly well and the phenomena are well described, which has not been the case earlier, cf. Hyensjö et al. (2007), paper 1. It seems that Hypothesis II gives the best correlation in these regions.

It was also established that the planar approach fails to predict fibre orientation in shear layers, *i.e.* the boundary layer and the wake regions. As emphasized in the theory section, the planar formulation (2.10) is strictly valid only if all fibres are oriented in the $x_1 - x_3$ plane, which is not the case in the shear layers. In the undisturbed region, the 3D and the planar approaches, agree in their results. This leads to the conclusion that both approaches are suitable when shear layers are not studied. After all, the planar approach requires less computational effort. On the other hand the fully 3D approach has much more information attached and different angles can be studied simultaneously, which can be helpful *e.g.* when conducting the design of experiments. As mentioned the lack of measurements for more accurately determining the parameters are needed. Moreover, measurements in turbulent shear flows are essential for further development of the models. Still, the method in this work is general in terms of having a one dispersion model working both in undisturbed regions and shear flows.

A possible extension to this work is to study the effects of the development











31

of a free jet and how this jet interacts with a moving solid web with different velocity. This will give even closer correlations to the final paper properties, although a strong coupling exists to the jet leaving the headbox. Additionally it is known that stiff slender fibres have a strong tendency to orient with the flow while flexible fibres do not. It would be interesting for further studies to develop the model to be valid for flexible fibres. Possibly, the level of rotational dispersion for flexible fibres are qualitatively in the same order of magnitude while the angular rotational velocities, *i.e.* the advection terms in fibre orientation space, are much lower.









Acknowledgements

During the completion of this doctoral thesis, several people have of course contributed to, influenced and supported my work in various ways. First of all, I would like to thank MetsoPaper Inc./Metso Academy and the Swedish Research Council for their financial support of the project. Next, I would like to thank my supervisor at the Royal Institute of Technology, Docent Anders Dahlkild, for his endless patience, support, assistance and guidance; our discussions have always been vivid, fruitful and interesting. Further, I would like to acknowledge my colleague and supervisor Dr Tomas Wikström of Metso Paper Inc, my colleagues and friends at Metso Paper Karlstad, and the people I have come into contact with at the Department of Mechanics and SFTI. Special thanks also go to my parents, Sylvi and Kalle, for their continuous support and their hospitality during my frequent stays at the final stage of this project. Finally, I would like to express my deepest thanks to my family Annie, Henrik and Carl without whose support, understanding, love and sacrifice this thesis would never have been completed.









Bibliography

- ADVANI, S. & TUCKER, C. 1987 The use of tensors to describe and predict fiber orientation in short fiber composites. *Journal of Rheology* **31** (8), 751–784.
- ASPLUND, G. & NORMAN, B. 2004 Fibre orientation anisotropy profile over the thickness of a headbox jet. J. Pulp Paper Sci. 30(8), 217–221.
- Bennington, C., Kerekes, R. & Grace, J. 1990 The yield stress of fibre suspensions,. *The Canadian Journal of chemical Engineering* **68**, 748–757.
- Carlsson, A., Lundell, F. & Söderberg, D. 2007 Fibre orientation control related to papermaking. *Journal of Fluids Engineering* **129** (4), 457–465.
- Drew, D. & Lahey, R. 1993 $Particulate\ Two-Phase\ Flow$, chap. 16, pp. 509–566. Butterworth-Heinemann, Boston.
- Enwald, H., Peirano, E. & Almstedt, A. E. 1996 Eulerian two-phase flow theory applied to fluidization. *Int. J. Multiphase Flow* **22**, 21–66.
- ERICSSON, K., TOLL, S. & MÅNSON, J.-A. 1997 The two-way interaction betwen anisotropic flow and fibre orientation in squeeze flow. *J. Rheology* **41** (3), 491–511.
- Goldsmith, H. & Mason, S. 1967 The Microrheology of Dispersions. In Rheology: Theory and Applications. Academic.
- Gullichsen, J. & Härkönen, E. 1981 Medium consistency technology part 1, fundamental data,. *Tappi* **64**, 69–72.
- HÄMÄLÄINEN, T. & HÄMÄLÄINEN, J. 2007 Modelling of fibre orientation in the headbox jet. J. Pulp Paper Sci. 31(1), 49–53.
- HOLM, R. 2005 Fluid mechanics of fibre suspensions related to papermaking. PhD thesis, Royal Institute of Technology (KTH), Stockholm, Sweden.
- Hyensjö, M., Dahlkild, A., Krochak, P., Olson, J. & Hämäläinen, J. 2007 Modelling the effect of shear flow on fibre orientation anisotropy in a planar contraction. *Nordic Pulp and Paper Research Journal* **22** (3), 376–382.
- Hyensjö, M., Dahlkild, A. & Wikström, T. 2008 Evolution of the rotational diffusivity coefficient of fibres along the centreline in turbulent planar contracting flows. *To be submitted*.
- Ishii, M. 1975 Thermo-fluid Dynamic Theory of Two-phase Flow. Eyrolles, Paris.
- JÄSBERG, J. 2007 Flow behaviour of fibre suspensions in straight pipes: New experimental techniques and multiphase modeling. PhD thesis, University of Jyväskylä.







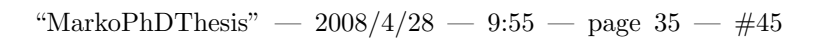


34 BIBLIOGRAPHY

- JEFFERY, G. 1922 The motion of ellipsoidal particles immersed in viscous fluid. Proc.R.Soc.Lond. A102, 161–179.
- Kerekes, R. & Schell, C. 1992 Characterization of fibre flocculation regimes by a crowding factor. *Journal of Pulp and Paper Science* **18** (1), J32–38.
- Leppänen, T., Erkkilä, A.-L., Sorvari, J. & Hämäläinen, J. 2005 Mathematical modelling of moisture induced out-of-plane deformation of a paper sheet. Modelling and Simulation in Materials Science and Engineering 13, 841–850.
- Lundell, F., Söderberg, D., Storey, S. & Holm, R. 2005 The effect of fibres on laminar-turbulent transistion and scales in turbulent decay. *Trans. 13th Fundamental Research Symposium, Oxford* 1, 19–34.
- MAXEY, M. & RILEY, J. 1983 Equation of motion for a small rigid sphere in a nonuniform flow. *Phys. Fluids* **26** (4), 883–889.
- NISKANEN, H., HÄMÄLÄINEN, T., ELORANTA, H., VAITTINEN, J. & HÄMÄLÄINEN, J. 2008 Dependence of fibre orientation on turbulence of the headbox flow. 94th Annual PAPTAC Meeting, Montreal.
- NORDSTRÖM, B. & NORMAN, B. 1994 Influence on sheet anisotropy, formation, z-toughness and tensile stiffness of reduced feed area to a headbox nozzle. *Nordic Pulp and Paper Research Journal* **1(9)**, 53–59.
- NORMAN, B. & SÖDERBERG, D. 2001 Overview of forming literature, 1990-2000. Trans. 12th Fundamental Research Symposium, Oxford 1, 431-558.
- OLSON, J. A. 2001 The motion of fibres in turbulent flow, stochastic simulation of isotropic homogeneous turbulence. *International Journal of Multiphase Flow* 27, 2083–2103.
- Olson, J. A., Frigaard, I., Chan, C. & Hämäläinen, J. P. 2004 Modelling a turbulent fibre suspension flowing in a planar contraction: The one-dimensional headbox. *International Journal of Multiphase Flow* **30**, 51–66.
- Olson, J. A. & Kerekes, R. J. 1998 The motion of fibres in turbulent flow. *Journal of Fluid Mechanics* 377, 47–64.
- Parsheh, M. 2001 Flow in contractions with application to headboxes. PhD thesis, Royal Institute of Technology, Stockholm, Sweden.
- Parsheh, M., Brown, M. & Aidun, C. 2005 On the orientation of stiff fibres suspended in turbulent flow in a planar contraction. *J. Fluid Mech.* **545**, 245–269
- Parsheh, M., Brown, M. & Aidun, C. 2006a Investigation of closure approximations for fiber orientation distribution in contracting turbulent flow. *J. Non-Newtonian Fluid Mech.* **136**, 38–49.
- Parsheh, M., Brown, M. & Aidun, C. 2006b Variation of fiber orientation in turbulent flow inside a planar contraction with different shapes. *International Journal of Multiphase Flow* 32, 1354–1369.
- ROACH, P. 1987 The generation of nearly isotropic turbulence by means of grids. Heat and Fluid Flow 8 (2), 82–92.
- Shin, M. & Koch, D. 2005 Rotational and translational dispersion of fibres in isotropic turbulent flows. *J. Fluid Mech.* **540**, 143–173.
- ULLMAR, M. 1997 Observations of fibre orientation in a headbox model at low consistency. *Tappi proceedings, Engineering and Papermakers Conference* p. 865.
- Ullmar, M. 1998 On fibre alignment mechanisms in a headbox nozzle. *Licentiate Thesis, Royal Institute of Technology, Stockholm, Sweden* .











BIBLIOGRAPHY 35

Wikström, T. & Rasmusson, A. 2002 Transition model and turbulence treatment of pulp suspension applied on a pressure screen. *Journal of Pulp and Paper Science* 28 (11), 374–378.

Zhang, X. 2001 Fibre orientation in a headbox. Masters Thesis, The University of British Columbia, Vancouver, Canada.







 "Marko Ph
D
Thesis" — 2008/4/28 — 9:55 — page 36 — #46



36 BIBLIOGRAPHY



